

Towards Efficient Integrated Perovskite/Organic Bulk Heterojunction Solar Cells: Interfacial Energetic Requirement to Reduce Charge Carrier Recombination Losses

Matyas Daboczi, Jinhyun Kim, Jinho Lee, Hongkyu Kang, Iain Hamilton, Chieh-Ting Lin, Stoichko D. Dimitrov, Martyn A. McLachlan, Kwanghee Lee, James R. Durrant, and Ji-Seon Kim*

Integrated perovskite/organic bulk heterojunction (BHJ) solar cells have the potential to enhance the efficiency of perovskite solar cells by a simple one-step deposition of an organic BHJ blend photoactive layer on top of the perovskite absorber. It is found that inverted structure integrated solar cells show significantly increased short-circuit current (J_{sc}) gained from the complementary absorption of the organic BHJ layer compared to the reference perovskite-only devices. However, this increase in J_{sc} is not directly reflected as an increase in power conversion efficiency of the devices due to a loss of fill factor. Herein, the origin of this efficiency loss is investigated. It is found that a significant energetic barrier (≈ 250 meV) exists at the perovskite/organic BHJ interface. This interfacial barrier prevents efficient transport of photogenerated charge carriers (holes) from the BHJ layer to the perovskite layer, leading to charge accumulation at the perovskite/BHJ interface. Such accumulation is found to cause undesirable recombination of charge carriers, lowering surface photovoltage of the photoactive layers and device efficiency via fill factor loss. The results highlight a critical role of the interfacial energetics in such integrated cells and provide useful guidelines for photoactive materials (both perovskite and organic semiconductors) required for high-performance devices.


1. Introduction

The rational design of device structures through optimized fabrication methods and materials selection has led to a remarkable increase in the power conversion efficiency (PCE) of perovskite solar cells, approaching 25% in the highest performing (typically mixed cation) devices.^[1–7] Although there is still room for further improvement in PCE in the single-junction perovskite solar cells,^[8,9] their efficiency is fundamentally limited by the Shockley–Queisser theoretical limit,^[10] for example at 30% PCE for the 1.6 eV bandgap methylammonium lead iodide (MAPI) layer.^[8,11,12]

On the other hand, multijunction solar cells consist of more than one photoactive semiconductor layers to absorb a wider wavelength range of the solar spectrum and can theoretically achieve a PCE in

M. Daboczi, Dr. J. Lee, Dr. I. Hamilton, Prof. J.-S. Kim
Department of Physics and Centre for Plastic Electronics
Imperial College London
London SW7 2AZ, UK
E-mail: ji-seon.kim@imperial.ac.uk

Dr. J. Kim, Dr. J. Lee, Dr. C.-T. Lin, Prof. J. R. Durrant
Department of Chemistry and Centre for Plastic Electronics
Imperial College London
London SW7 2AZ, UK

 The ORCID identification number(s) for the author(s) of this article can be found under <https://doi.org/10.1002/adfm.202001482>.

© 2020 The Authors. Published by WILEY-VCH Verlag GmbH & Co. KGaA, Weinheim. This is an open access article under the terms of the Creative Commons Attribution License, which permits use, distribution and reproduction in any medium, provided the original work is properly cited.

DOI: 10.1002/adfm.202001482

Dr. J. Lee, Dr. H. Kang, Prof. K. Lee
Heeger Center for Advanced Materials and Research Institute for Solar and Sustainable Energies
Gwangju Institute of Science and Technology
Gwangju 61005, Republic of Korea

Dr. C.-T. Lin, Dr. M. A. McLachlan
Department of Materials and Centre for Plastic Electronics
Imperial College London
London SW7 2AZ, UK

Dr. S. D. Dimitrov, Prof. J. R. Durrant
SPECIFIC
College of Engineering
Swansea University
Bay Campus, Swansea SA1 8EN, UK

Dr. S. D. Dimitrov
School of Biological and Chemical Sciences
Queen Mary University of London
Mile End Road, London E1 4NS, UK

excess of 40%.^[13,14] Applying a large bandgap perovskite top cell either on silicon,^[15,16] on Cu(In,Ga)Se₂,^[17,18] or even on a smaller bandgap perovskite layer^[19–23] has been demonstrated to be a promising approach towards cost-effective, high efficiency, and sustainable tandem solar cells,^[24,25] with a record 28% certified PCE achieved for perovskite-silicon tandem devices.^[26] Disadvantages of these tandem devices include the requirement for a recombination layer between the two photoactive layers and the necessity of matching the generated photocurrents of the bottom and top cells.^[27]

To overcome some of these limitations in multijunction solar cells, an integrated perovskite/bulk heterojunction (BHJ) solar cell (referred to here as the integrated cell) approach has been taken, in which a narrow bandgap organic semiconductor-based BHJ layer is deposited directly on top of a larger bandgap perovskite layer in order to harvest both the visible and near-infrared parts of the solar spectrum.^[28–30] The integrated cell is similar to a perovskite/polymer tandem cell,^[31] but without the need for a recombination layer or matching of photocurrents, enabling an easier and cheaper fabrication process of flexible, lightweight, and printable devices.^[32–34] MAPI based integrated cells with both conventional (n–i–p) and inverted (p–i–n) device structures were demonstrated^[35,36] with the highest PCE (19.0%) reported in the conventional structure integrated cell.^[36] However, this PCE is still lower than the 21.2% efficiency achieved with a pure MAPI perovskite device.^[37] This suggests that detailed understanding of the efficiency loss mechanism in the integrated cells is urgently needed in order to achieve high performance devices closer to the single-junction Shockley–Queisser limit.

The fundamental understanding of efficiency losses can be obtained via thorough investigation of photogenerated charge carriers using a range of energetic and transient spectroscopic techniques. Ultrafast transient absorption spectroscopy (uf-TAS) is an optical technique that can give information on charge carrier trapping, transfer and recombination in semiconductors and has been applied widely to study both organic^[38–40] and perovskite devices.^[41–43] Surface photovoltage (SPV) is a contactless way of measuring the change in surface potential of a sample upon light illumination. The redistribution of photogenerated charge carriers, which is required for the formation of SPV, is governed by the potential difference present in the material at the surface and also at the buried interfaces.^[44,45] Therefore, the sign, magnitude, and dynamics of the measured SPV can reveal information on the nature of charge carriers and the presence of charge trapping, accumulation, and recombination. SPV has been used extensively to characterize inorganic materials^[46] and more recently on both organic^[47] and hybrid organic–inorganic perovskite photoactive materials.^[48–50] An important feature of this technique is that it is not confined to measuring a full device, allowing the study of charge carrier transport and accumulation at different materials and interfaces, hence providing a powerful tool to probe efficiency loss mechanisms in photovoltaic devices, which we demonstrate in this work.

Herein, we first fabricate inverted structure integrated cells applying MAPI and organic BHJ layer composed of a narrow bandgap polymer (TT) and PCBM. We achieve a PCE of 17.7% with these integrated cells, which is higher than PCEs reported previously (16.4%) with the same p–i–n device structure and

same BHJ layer.^[35] However, we notice that despite the significant increase in short-circuit current density (J_{sc}) from 19.9 mA cm⁻² to 22.1 mA cm⁻², the PCE of the integrated cells is only slightly higher than the reference MAPI devices due to the presence of undesirable losses within the integrated cells, in particular a reduced fill factor (FF). By applying ambient photoemission spectroscopy (APS) and Kelvin probe to measure the electronic energy levels, uf-TAS to probe charge carrier dynamics and SPV to detect interfacial charge carrier recombination, we identify the main PCE loss mechanism. We measure a \approx 250 meV energetic barrier for hole transport formed at the interface between the organic BHJ and MAPI layers that leads to interfacial charge carrier accumulation and recombination. These observations elucidate one of the important loss mechanisms in integrated perovskite/BHJ devices and suggest a potential method (by proper energy level tuning of the photoactive layers) to further improve device performance.

2. Results and Discussion

2.1. Structure and Performance of Integrated Perovskite/BHJ Solar Cell

The integrated cell used for this work was developed based on an inverted perovskite device structure applying indium tin oxide (ITO) as an anode, polytriarylamine (PTAA) as hole transport layer (HTL), poly[(9,9-bis(3'-(N,N-dimethylamino)propyl)-2,7-fluorene)-alt-2,7-(9,9-dioctylfluorene)] (PFN) polymer layer as interfacial compatibiliser, MAPI as the photoactive layer (1.60 eV bandgap), PCBM and a thin layer of ZnO nanoparticles as electron transport layers (ETLs) and finally a silver cathode. In the integrated cell, the PCBM layer was replaced with a ternary BHJ blend composed of the TT narrow bandgap (1.37 eV) polymer (16 w/w%), PCBM (80 w/w%), and N2200 (4 w/w%) to give the final structure of the integrated cell as illustrated in **Figure 1a**.

The current-voltage characteristic curves and external quantum efficiency (EQE) spectra of the highest performing MAPI perovskite-only device (with PCBM ETL) compared to the champion integrated cell (with optimized BHJ layer) are shown in **Figure 1c,d**. The spectra show similarly high EQE (70–80%) for both devices in the wavelength range of 400–800 nm, and for the integrated cell an EQE reaching up to 40% in the 800–900 nm wavelength range as evidence of short-circuit current being generated due to the absorption of TT in the BHJ layer (see **Figure 1b** for absorption spectra). As a result of the extended absorption, an increase of more than 10% in the short-circuit current is observed in the integrated cell (-22.1 mA cm⁻²) compared to the perovskite-only cell (-19.9 mA cm⁻²).

The characteristic values for both the perovskite and integrated cells are compared in **Table 1**. Interestingly, the relatively high V_{oc} of the perovskite cells (1.11 V) is maintained in the integrated cells (1.10 V) in spite of the low V_{oc} (0.68 V) of the organic BHJ only cells (see **Figure S1** in the Supporting Information). This suggests that the V_{oc} of the integrated cell is dominated by the perovskite photoactive layer, consistent with most of the photocurrent generation happening in the MAPI layer (see **Figure 1d**), which can explain the quasi-Fermi levels being pinned to the perovskite layer.^[51]

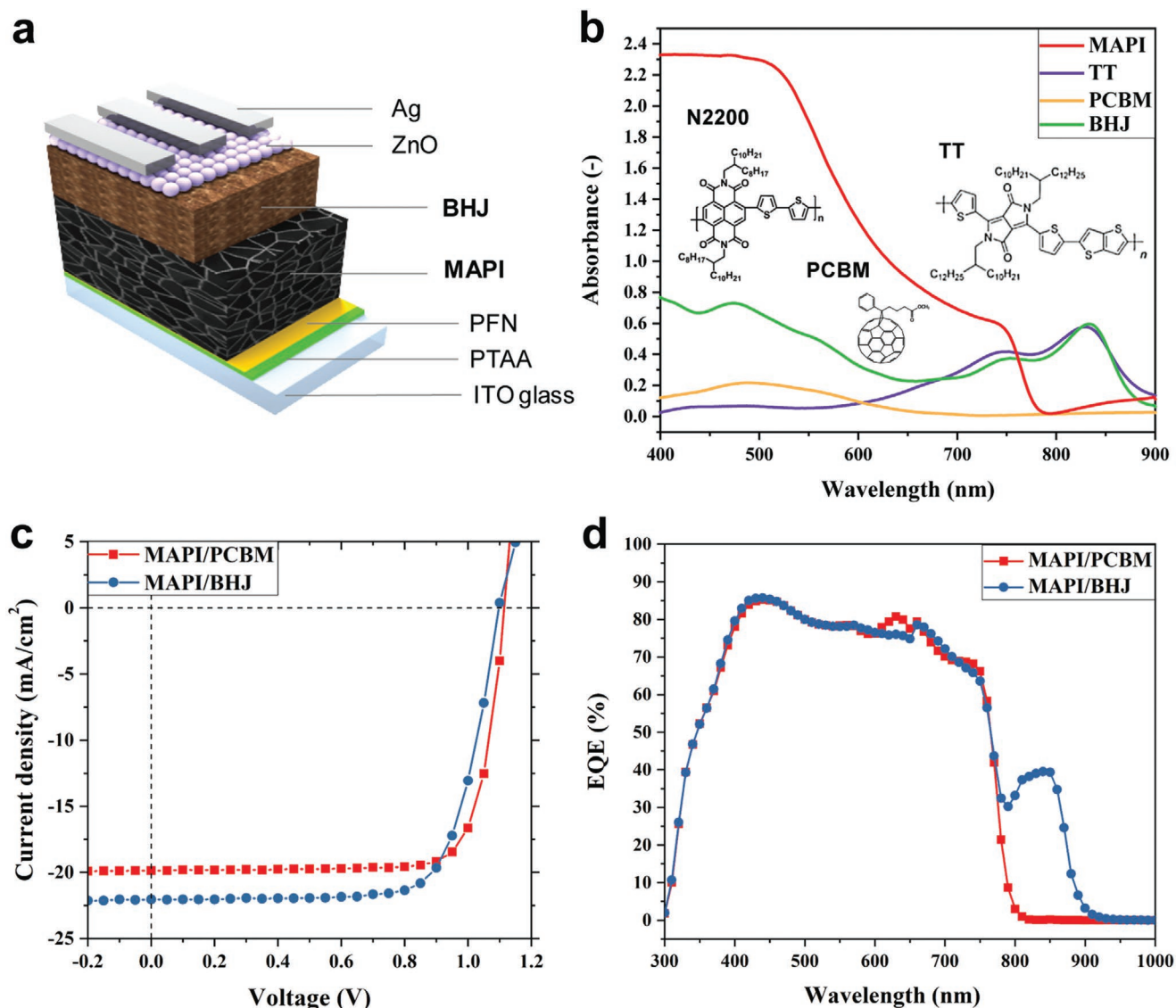


Figure 1. Structure and performance of integrated perovskite/bulk heterojunction solar cell. a) Inverted device structure and b) absorption spectra of the constituent photoactive layers and chemical structure for the constituents of the BHJ layer. c) Current–voltage scans under 1 sun equivalent illumination and d) EQE spectra of MAPI/PCBM perovskite device (red curves) compared to MAPI/BHJ integrated solar cell (blue curves).

The high V_{oc} and J_{sc} with FF of 0.73 resulted in a champion PCE of 17.7% (average 16.7%), which is a noticeable improvement compared to the previously reported values (champion PCE of 16.4% with average of 16.2%) applying the same TT polymer in an integrated cell;^[35] this is mainly due to the optimization of device interlayers. However, in spite of increased

Table 1. Photovoltaic performance of champion perovskite device with PCBM and champion integrated cell with BHJ layer. The average performance of several devices is shown in brackets.

	J_{sc} [mA cm^{-2}]	V_{oc} [V]	FF [-]	PCE [%]
MAPI/PCBM	-19.87 (-19.24)	1.11 (1.10)	0.79 (0.77)	17.5 (16.3)
MAPI/BHJ	-22.05 (-21.41)	1.10 (1.10)	0.73 (0.70)	17.7 (16.7)

J_{sc} , the PCE of integrated cells only slightly exceeds the performance of the reference perovskite-only devices (champion PCE of 17.5%, average of 16.3%) due to FF dropping from 0.79 (average of 0.77) to 0.73 (average of 0.70). If there was no FF drop a significantly higher PCE (>19%) would be expected in these integrated cells. We note that the devices showed only very minimal hysteresis with no significant change in FF or PCE between forward and reverse scans (see Figure S3 in the Supporting Information). The steady state PCE, J_{sc} are shown in Figure S4 in the Supporting Information and the average current–voltage curves and their characteristic values are presented in Figure S2 and Table S1 in the Supporting Information showing the same trends as discussed for the champion cells. The decreased FF suggests extra losses in the integrated cell, the origin of which is investigated below.

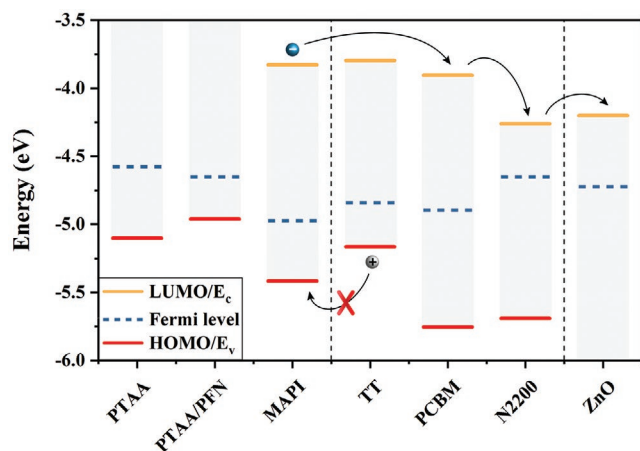


Figure 2. Energy level diagram for all layers of the integrated cell. The energy bands for the constituent layers of the ternary blend are divided by vertical dashed lines.

2.2. Energy Levels for Constituent Layers of Integrated Cell

In order to understand the contribution of the different photoactive and transport materials we built up the device layer-by-layer and performed energy level, transient absorption, and SPV measurements. The energy levels for the constituent layers are shown in **Figure 2**, which also includes the separate organic materials used for the ternary BHJ blend. The values of highest occupied molecular orbital (HOMO) for organic layers and valence band edge (E_v) for the inorganic semiconductors were determined by APS, the Fermi levels (E_F) were measured by Kelvin probe, while the lowest unoccupied molecular orbital (LUMO) or the conduction band edge (E_c) values were calculated by adding the optical bandgap to the HOMO value. The stable E_F measurements and the APS spectra are shown in Figures S5 and S6 in the Supporting Information and the measured and calculated values are summarized in Table S2 in the Supporting Information.

The measured energy levels (**Figure 2**) show an E_v of -5.42 eV for MAPI and a HOMO of -5.17 eV for TT which are in good agreement with previously reported values.^[35,52] These energy level values indicate no energetic impediment for the transport of holes and electrons that were generated in the perovskite layer, especially considering the high ratio (80 w/w%) of PCBM in the ternary blend. On the other hand, when charge carriers are generated in the organic BHJ layer, an efficient hole transport to MAPI is inhibited due to a ≈ 250 meV energy barrier present between the HOMO of the TT polymer and the E_v of the perovskite layer. Due to the presence of this energetic barrier, holes can accumulate at the MAPI/BHJ interface leading to undesirable recombination losses in the integrated cells. We measure these losses and discuss below the impact that they have on device performance.

2.3. Charge Transfer and Charge Carrier Recombination at MAPI/BHJ Interface

In order to investigate potential recombination losses due to inhibited hole transfer from TT in the organic BHJ layer to

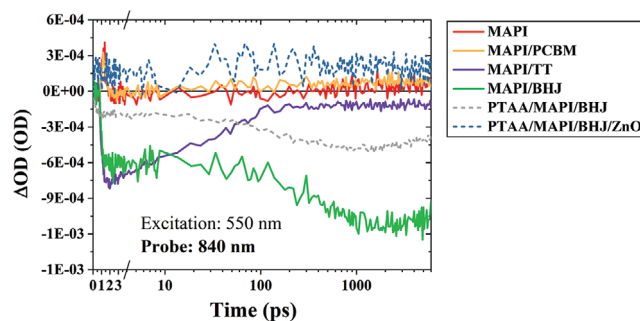


Figure 3. Transient absorption kinetics of the perovskite and bulk hetero-junction layers with excitation at 550 nm. The excited charge carriers in TT are probed at a laser wavelength of 840 nm. Solid lines show spectra for single and double layers on soda lime glass, dashed lines correspond to almost complete devices built on ITO.

MAPI layer in the integrated cell, we carried out uf-TAS measurements. An excitation source at a wavelength of 550 nm was used, allowing for charge carrier generation in both MAPI and BHJ photoactive layers, with excitation from the MAPI side. The change in optical density (ΔOD) on the femtosecond time-scale was tracked separately for MAPI with a probe wavelength at 760 nm, and for TT at 840 nm, tracking in both cases the ground state bleaching (GSB)/stimulated emission signals of these materials.^[41,53] **Figure 3** shows that there is negligible change in ΔOD for MAPI films alone at 840 nm, in agreement with the lack of MAPI ground state absorption at this wavelength. However, there is a significant GSB signal at 840 nm for MAPI/TT and MAPI/BHJ films, indicating the presence of TT photoinduced excited states or charge carriers. 3D plots of the uf-TAS spectra, showing also excited-state absorption features at 900 and 1100 nm, are displayed in Figure S7 in the Supporting Information. Similar TT GSB signals were observed following direct excitation of TT at 840 nm (**Figure S8**, Supporting Information), confirming this signal arises primarily from direct excitation of TT.

The TT ground state bleach/stimulated emission signal observed at 840 nm for the MAPI/TT film excited at 550 nm largely decays with 100 ps (**Figure 3**), assigned to TT exciton decay to ground. Consistent with this assignment, a similar decay was observed for TT films alone excited at 840 nm (**Figure S8**, Supporting Information). No corresponding rise of MAPI signal at 760 nm was observed, (**Figure S7**, Supporting Information), confirming the decay at 840 nm does not arise for energy or charge transfer from TT to MAPI. In contrast, the 840 nm signal observed following 550 nm excitation of MAPI/BHJ films does not decay, but rather shows a growth in amplitude with a time constant of ≈ 500 ps (**Figure 3**, green line; **Figure S7**, Supporting Information). This signal growth was not observed for direct excitation of the TT:PCBM BHJ at 840 nm for samples both with and without MAPI underlayer (see 3D uf-TAS spectra in **Figure S8** in the Supporting Information). This growth is therefore assigned to energy or, more likely, charge transfer from MAPI to TT, enabled by the presence of PCBM in the BHJ blend. This charge transfer from MAPI to TT is striking and suggests the presence of PCBM impacts on the energetics of the MAPI/organic interface. It is tentatively assigned to electron accumulation on the PCBM, most likely

induced by light irradiation, which results in a modulation of the MAPI/TT interfacial energetics to enable hole transfer from MAPI to TT. Supporting this conclusion, we observed that this rise in TT bleaching TAS signal is less significant when the MAPI/BHJ bilayer is deposited on PTAA, attributed to kinetic competition between hole transfer from MAPI to PTAA and TT (Figure 3, dashed grey line). Further supporting this conclusion, the TT GSB signal is fully suppressed for the full stack with ZnO top layer, most likely resulting from electron extraction from PCBM to ZnO which could remove the shift in interfacial energetics favoring hole transfer from MAPI to TT observed for MAPI/BHJ films. Whilst a full analysis of the charge carrier dynamics in these multilayer films is beyond the scope of this study, these uf-TAS data do indicate that charge transfer dynamics between MAPI and TT depends on the details of the overall device stack, indicative of shifts in energetics at the MAPI/organic interface. We also note that the direction of hole transfer we observed (from MAPI to TT) in the MAPI/BHJ bilayer is the reverse of that required to drive the enhanced photocurrent generation in complete devices, further emphasizing that the interfacial charge transfer is likely to be substantially influenced by charge accumulation in the complete device.

In order to further investigate the interfacial energetics and recombination losses in the integrated cell, we performed SPV measurements, starting from MAPI layer alone on top of HTL (PTAA/PFN) layer and building layer-by-layer the different top layers. Figure 4a shows the magnitude and dynamics of SPV generated by illuminating the samples with white light for 100 s. The difference in work function measured under illumination (WF_{light}) and in dark (WF_{dark}) determines the sign and magnitude of the generated SPV: ($\Delta WF = WF_{\text{light}} - WF_{\text{dark}}$).

All samples show positive SPV signals, indicating an increased density of electrons on the surface of the samples under illumination, which is a clear sign of effective hole extraction from the photoactive layers to the PTAA/PFN layer.^[44,54]

After turn-on of light, the SPV signal increases slowly in the seconds timescale for the MAPI only sample, indicating slow redistribution of ions present in the perovskite layer.^[55–57]

The magnitude of SPV reaches ≈ 210 meV for MAPI and is increased to ≈ 245 mV with a top electron transporting PCBM layer. Importantly, the SPV value drops significantly down to ≈ 150 meV (40% drop compared to PCBM only layer) for the MAPI sample with the organic BHJ layer on top (still 80% of PCBM) and is increased to ≈ 290 mV with ZnO electron extracting layer. Such a significant drop in SPV observed for the MAPI/BHJ sample indicates a large loss of photogenerated charge carriers at the MAPI/BHJ interface.

In order to understand such loss of photogenerated charge carriers, the energy level alignment is considered (Figure 4b,c) based on the measured E_F and E_v or HOMO of MAPI, TT, and PCBM and their interfaces (see Figure 2). For an efficient integrated device, holes photogenerated in the organic BHJ layer (i.e., in TT polymer) should be transported from TT towards the MAPI/TT interface to be extracted by the HTL underneath. However, due to the 250 meV energetic barrier the hole transport is now strongly inhibited and accumulation of holes can occur at the MAPI/BHJ interface. This hole accumulation, together with unwanted hole transfer from MAPI to TT, will lead to nonradiative recombination with the electrons existing in the BHJ layer. Such undesirable recombination of charge carriers will reduce the total density of electrons present in the BHJ layer and hence significantly lower SPV values measured for the MAPI/BHJ sample. This observation is fully consistent with the lack of effective hole transfer from TT to MAPI probed by the uf-TAS measurements (Figure 3).

We consider the effect of surface morphology on the measured SPV (slightly smaller SPV with rougher surface is expected). However, our morphology measurements show much smoother surface for the MAPI/BHJ sample (RMS roughness of 7.0 nm) than for the MAPI only sample (RMS roughness of 14.6 nm) (Figures S9 and S10, Supporting

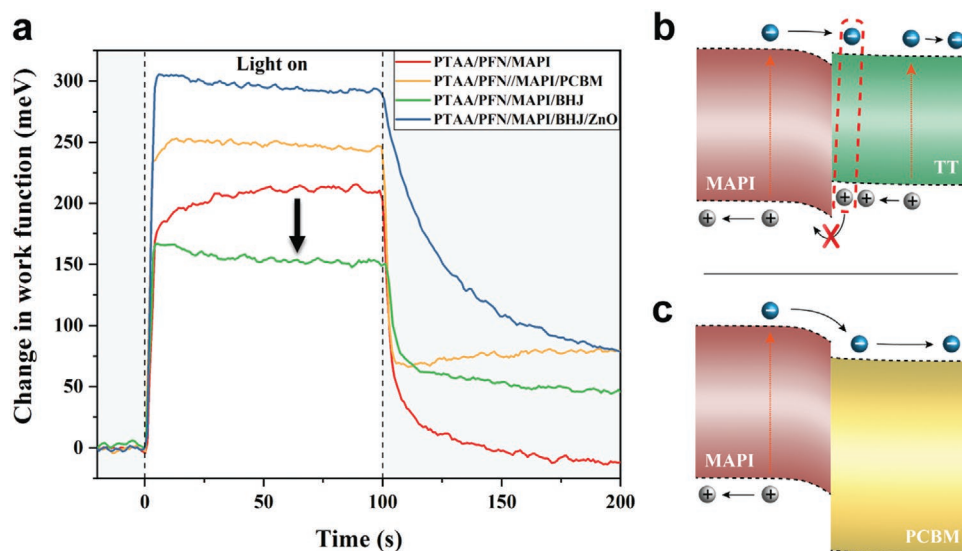


Figure 4. Surface photovoltage measurements and illustration of interfacial charge transfer and recombination. a) Magnitude and dynamics of surface photovoltage comparing MAPI without ETL to MAPI with PCBM or BHJ and to an almost finished device with ZnO ETL. b) Illustration of hole accumulation and charge carrier recombination (indicated with red dashed box) at MAPI/TT, c) but quick and efficient electron transfer at MAPI/PCBM interface.

Information), excluding the surface morphology as a main cause for the reduced SPV.

After turning the light off, there is a fast decay of SPV signal (fast recombination of charge carriers) followed by much slower decay. The slow SPV decay is most likely originated from redistribution ions^[58] in MAPI and slow recombination of trapped charges.^[59,60] The latter cause becomes more significant with the ZnO top layer, in which a significant amount of defect states are present.^[61]

In a working integrated cell, the hole accumulation due to the energetic barrier at the MAPI/TT interface (see Figure 4b) is expected to become significant at voltages close to open-circuit condition, and so such accumulation-induced loss mainly appears as a drop in FF (see Table 1). It is also reflected in the continuous increase of current density towards short-circuit condition (i.e., lowering applied voltages, 0–0.8 V) for the integrated cell (see Figure S2 in the Supporting Information), resulting in a lower shunt resistance ($810 \Omega \text{ cm}^{-2}$) compared to the perovskite-only devices ($2560 \Omega \text{ cm}^{-2}$).

3. Conclusion

In summary, we investigated the origin of efficiency losses in an inverted structure integrated perovskite/BHJ solar cells. We found that a significant energetic barrier ($\approx 250 \text{ meV}$) is present at the perovskite/organic BHJ interface. This interfacial barrier is found to prevent efficient transport of photogenerated charge carriers (holes) from the BHJ layer to the perovskite layer, as probed by ultrafast transient absorption spectroscopy. It leads to hole accumulation at the perovskite/BHJ interface, causing undesirable recombination of charge carriers and thus lowering surface photovoltage of the photoactive layers and device efficiency via fill factor loss. Our results highlight the importance of interfacial energetics in integrated cells and provide useful guidelines for photoactive materials (both perovskite and organic semiconductors) towards high device performance. For example, a strategy to eliminate the energetic barrier for efficient charge transport can be to utilize a perovskite layer with shallower E_v while keeping its large optical bandgap or to retain MAPI but apply a narrow bandgap polymer with HOMO level deeper than the E_v of MAPI (-5.4 eV).

4. Experimental Section

Sample and Device Preparation: ITO substrates were cleaned by sequential sonication (10 min for each step) in distilled water, acetone, and 2-propanol, finally dried in an oven and UV-ozone treated for 20 min before layer deposition. The reference perovskite cell was prepared in a nitrogen filled glovebox with a structure of ITO/PTAA(10 nm)/PFN(5 nm)/MAPI(350 nm)/PCBM(30 nm)/ZnO(20 nm)/Ag, where PTAA is polytriarylamine, PFN is poly[(9,9-bis(3'-(N,N-dimethylamino)propyl)-2,7-fluorene)-alt-2,7-(9,9-dioctylfluorene)], PCBM is [6,6]-Phenyl-C61-butyric acid methyl ester, while ZnO and Ag stand for zinc oxide and silver respectively. Solutions of 2 mg mL⁻¹ in toluene for PTAA and 0.4 mg mL⁻¹ in methanol for PFN were used. The thin polymer layers of PTAA (EM Index) and PFN (1-Material) were spun at 5000 rpm for 15 s. The MAPI layer was prepared by spin-coating a 1.5 M precursor solution (1:1 ratio of lead iodide (Alfa Aesar) and methylammonium iodide (Dyesol) in the mixture of N,N-dimethylformamide/dimethylsulfoxide = 9/1.1)

at 4000 rpm for 30 s, with diethyl ether antisolvent dripping at 7s. The ITO/PTAA/PFN/MAPI layers were annealed at 100 °C for 10 min before depositing the PCBM (Ossila) layer from a 30 mg mL⁻¹ chlorobenzene based solution with a spinning speed of 1500 rpm. Finally a thin layer of ZnO was spun at 5000 rpm from a 1 wt% ZnO nanoparticle dispersion (NCT) in 2-propanol and the device was finished with the evaporation of 100 nm silver electrode. The integrated cell was prepared the same way as the reference device, except instead of the PCBM a BHJ layer was deposited on top of MAPI at 1000 rpm spin rate resulting in an optimized thickness of around 200 nm. The precursor solution of the ternary BHJ blend was prepared by dissolving 4 mg DT-PDPP2T-TT (TT) low bandgap polymer, 20 mg PCBM and 1 mg poly[[N,N'-bis(2-octyl-dodecyl)-naphthalene-1,4,5,8-bis(dicarboximide)-2,6-diy]-alt-5,5'-(2,2'-bithiophene)] (N2200) in 2.67 mL mixture of chloroform (97%) and diphenyl ether (3%). Samples for energy level and SPV measurements up to the specified final layer were prepared the same way. Thin layers were deposited on soda lime glass for uf-TAS.

Solar Cell Characterization: The current–voltage curves for the reference MAPI and integrated solar cells were measured in a nitrogen filled glovebox under 1 sun equivalent illumination intensity (100 mW cm^{-2}) generated by a xenon light source (150 W Oriel) and calibrated by a silicon reference cell certified by the National Renewable Energy Laboratory. A Keithley 236 Source Measure unit was used to record the current and scan the voltage from 1.2 to -0.2 V with 100 mV s^{-1} scan rate. EQE measurements were performed using a QEX10 system (PV Measurements, Inc.).

Optical Characterization: Absorption spectra of the thin films were measured by a Shimadzu UV-2600 UV–vis spectrophotometer. A transient absorption spectrometer (HELIOS, Ultrafast system) was used to perform uf-TAS measurements, which had an instrument response time of approximately 200 fs, using an imaging spectrometer with white light probe (450–1450 nm) to record the transient spectra. The excitation light (550 and 840 nm) for uf-TAS measurements was generated by an 800 nm wavelength Solstice (Newport Corporation) Ti:sapphire regenerative amplifier at a 1KHz repetition rate and a TOPAS-Prime (light conversion) optical parametric amplifier. The excitation fluence was set to 1 and $5 \mu\text{J cm}^{-3}$ by applying a graded neutral density filter.

Energy Level and SPV Measurements: Energy level measurements were carried out with an APS04 system (KP Technology), which includes a Kelvin probe with 2 mm gold alloy vibrating tip. The contact potential difference with respect to the tip work function was measured for all samples in dark until equilibrium was reached (10–60 min). The tip's work function was determined before the measurements using a cleaned silver reference and used to calculate the absolute value of work function for the samples. The samples were illuminated with white light by a quartz tungsten halogen light source (Dolan–Jenner) at 20 mW cm^{-2} intensity for 100 s in order to measure SPV. HOMO/ E_v of the samples were determined by APS, scanning the energy of the UV light source in the 4.6–6.0 eV range and by plotting and extrapolating to zero the cube root of the photoemission signal.

Supporting Information

Supporting Information is available from the Wiley Online Library or from the author.

Acknowledgements

The authors acknowledge the funding of UK Engineering and Physical Sciences Research Council (EPSRC) Plastic Electronics Doctoral Training Centre (EP/L016702/1) and KP Technology Ltd for a CASE studentship. SD's contribution is part funded by the European regional Development Fund through the Welsh Government. Support from the Global Research Laboratory Program of the National Research Foundation (NRF) funded by the Ministry of Science, ICT & Future Planning (NRF-2017K1A1A2013153) is greatly acknowledged.

Conflict of Interest

The authors declare no conflict of interest.

Keywords

bulk heterojunctions, integrated cell, perovskites, photovoltages, solar cells, transient optical spectroscopy

Received: February 14, 2020

Revised: March 13, 2020

Published online:

- [1] A. Kojima, K. Teshima, Y. Shirai, T. Miyasaka, *J. Am. Chem. Soc.* **2009**, *131*, 6050.
- [2] H. S. Kim, C. R. Lee, J. H. Im, K. B. Lee, T. Moehl, A. Marchioro, S. J. Moon, R. Humphry-Baker, J. H. Yum, J. E. Moser, M. Grätzel, N. G. Park, *Sci. Rep.* **2012**, *2*, 591.
- [3] P. Docampo, J. M. Ball, M. Darwich, G. E. Eperon, H. J. Snaith, *Nat. Commun.* **2013**, *4*, 2761.
- [4] M. Liu, M. B. Johnston, H. J. Snaith, *Nature* **2013**, *501*, 395.
- [5] M. Saliba, T. Matsui, J. Y. Seo, K. Domanski, J. P. Correa-Baena, M. K. Nazeeruddin, S. M. Zakeeruddin, W. Tress, A. Abate, A. Hagfeldt, M. Grätzel, *Energy Environ. Sci.* **2016**, *9*, 1989.
- [6] W. S. Yang, B. W. Park, E. H. Jung, N. J. Jeon, Y. C. Kim, D. U. Lee, S. S. Shin, J. Seo, E. K. Kim, J. H. Noh, S. Il Seok, *Science* **2017**, *356*, 1376.
- [7] N. J. Jeon, H. Na, E. H. Jung, T. Y. Yang, Y. G. Lee, G. Kim, H. W. Shin, S. Il Seok, J. Lee, J. Seo, *Nat. Energy* **2018**, *3*, 682.
- [8] W. Tress, *Adv. Energy Mater.* **2017**, *7*, 1602358.
- [9] M. Saliba, J. P. Correa-Baena, M. Grätzel, A. Hagfeldt, A. Abate, M. Gr. A. Hagfeldt, A. Abate, *Angew. Chem., Int. Ed.* **2018**, *57*, 2554.
- [10] W. Shockley, H. J. Queisser, *J. Appl. Phys.* **1961**, *32*, 510.
- [11] W. E. I. Sha, X. Ren, L. Chen, W. C. H. Choy, *Appl. Phys. Lett.* **2015**, *106*, 221104.
- [12] S. Rühle, *Sol. Energy* **2016**, *130*, 139.
- [13] F. H. Alharbi, S. Kais, *Renewable Sustainable Energy Rev.* **2015**, *43*, 1073.
- [14] Z. J. Yu, M. Leilaieoun, Z. Holman, *Nat. Energy* **2016**, *1*, 1.
- [15] B. Chen, Z. Yu, K. Liu, X. Zheng, Y. Liu, J. Shi, D. Spronk, P. N. Rudd, Z. Holman, J. Huang, *Joule* **2019**, *3*, 177.
- [16] J. Werner, L. Barraud, A. Walter, M. Bräuninger, F. Sahli, D. Sacchetto, N. Tétreault, B. Paviet-Salomon, S. J. Moon, C. Allebé, M. Despeisse, S. Nicolay, S. De Wolf, B. Niesen, C. Ballif, *ACS Energy Lett.* **2016**, *1*, 474.
- [17] F. Fu, T. Feurer, T. P. Weiss, S. Pisoni, E. Avancini, C. Andres, S. Buecheler, A. N. Tiwari, *Nat. Energy* **2017**, *2*, 1.
- [18] Q. Han, Y. T. Hsieh, L. Meng, J. L. Wu, P. Sun, E. P. Yao, S. Y. Chang, S. H. Bae, T. Kato, V. Bermudez, Y. Yang, *Science* **2018**, *361*, 904.
- [19] D. P. McMeekin, G. Sadoughi, W. Rehman, G. E. Eperon, M. Saliba, M. T. Hörantner, A. Haghighirad, N. Sakai, L. Korte, B. Rech, M. B. Johnston, L. M. Herz, H. J. Snaith, *Science* **2016**, *351*, 151.
- [20] D. Zhao, Y. Yu, C. Wang, W. Liao, N. Shrestha, C. R. Grice, A. J. Cimaroli, L. Guan, R. J. Ellingson, K. Zhu, X. Zhao, R.-G. Xiong, Y. Yan, *Nat. Energy* **2017**, *2*, 17018.
- [21] D. Forgács, L. Gil-Escrig, D. Pérez-Del-Rey, C. Momblona, J. Werner, B. Niesen, C. Ballif, M. Sessolo, H. J. Bolink, *Adv. Energy Mater.* **2017**, *7*, 1.
- [22] J. Ávila, C. Momblona, P. Boix, M. Sessolo, M. Anaya, G. Lozano, K. Vandewal, H. Míguez, H. J. Bolink, *Energy Environ. Sci.* **2018**, *11*, 3292.
- [23] D. P. McMeekin, S. Mahesh, N. K. Noel, M. T. Klug, J. Lim, J. H. Warby, J. M. Ball, L. M. Herz, M. B. Johnston, H. J. Snaith, *Joule* **2019**, *3*, 1.
- [24] H. J. Snaith, *Nat. Mater.* **2018**, *17*, 372.
- [25] Q. Wali, N. K. Elumalai, Y. Iqbal, A. Uddin, R. Jose, *Renewable Sustainable Energy Rev.* **2018**, *84*, 89.
- [26] National Renewable Energy Laboratory, "Best Research-Cell Efficiencies," can be found under, <https://www.nrel.gov/pv/assets/pdfs/pv-efficiency-chart.20190103.pdf>, **2019**.
- [27] J. Werner, B. Niesen, C. Ballif, *Adv. Mater. Interfaces* **2018**, *5*, 1700731.
- [28] C. Zuo, L. Ding, *J. Mater. Chem. A* **2015**, *3*, 9063.
- [29] L. Ye, B. Fan, S. Zhang, S. Li, B. Yang, Y. Qin, H. Zhang, J. Hou, *Sci. China Mater.* **2015**, *58*, 953.
- [30] Y. Liu, Y. Chen, *Adv. Mater.* **2020**, *32*, 1.
- [31] Y. Liu, L. A. Renna, M. Bag, Z. A. Page, P. Kim, J. Choi, T. Emrick, D. Venkataraman, T. P. Russell, *ACS Appl. Mater. Interfaces* **2016**, *8*, 7070.
- [32] P. Jiang, T. W. Jones, N. W. Duffy, K. F. Anderson, R. Bennett, M. Grigore, P. Marvig, Y. Xiong, T. Liu, Y. Sheng, L. Hong, X. Hou, M. Duan, Y. Hu, Y. Rong, G. J. Wilson, H. Han, *Carbon* **2018**, *129*, 830.
- [33] N. Torabi, A. Behjat, Y. Zhou, P. Docampo, R. J. Stoddard, H. W. Hillhouse, T. Ameri, *Mater. Today Energy* **2019**, *12*, 70.
- [34] Y. Liu, Z. Hong, Q. Chen, W. Chang, H. Zhou, T. Bin Song, E. Young, Y. Yang, J. You, G. Li, Y. Yang, *Nano Lett.* **2015**, *15*, 662.
- [35] J. Kim, G. Kim, H. Back, J. Kong, I. W. Hwang, T. K. Kim, S. Kwon, J. J. H. Lee, J. J. H. Lee, K. Yu, C. L. Lee, H. Kang, K. Lee, *Adv. Mater.* **2016**, *28*, 3159.
- [36] K. Gao, Z. Zhu, B. Xu, S. B. Jo, Y. Kan, X. Peng, A. K. Y. Jen, *Adv. Mater.* **2017**, *29*, 1703980.
- [37] S. S. Shin, E. J. Yeom, W. S. Yang, S. Hur, M. G. Kim, J. Im, J. Seo, J. H. Noh, S. Il Seok, *Science* **2017**, *356*, 167.
- [38] C. G. Shuttle, B. O'Regan, A. M. Ballantyne, J. Nelson, D. D. C. Bradley, J. R. Durrant, *Phys. Rev. B* **2008**, *78*, 113201.
- [39] K. Kawashima, Y. Tamai, H. Ohkita, I. Osaka, K. Takimiya, *Nat. Commun.* **2015**, *6*, 10085.
- [40] H. Cha, J. Wu, A. Wadsworth, J. Nagitta, S. Limbu, S. Pont, Z. Li, J. Searle, M. F. Wyatt, D. Baran, J. S. Kim, I. McCulloch, J. R. Durrant, *Adv. Mater.* **2017**, *29*, 1.
- [41] G. Xing, N. Mathews, S. Sun, S. S. Lim, Y. M. Lam, M. Grätzel, S. Mhaisalkar, T. C. Sum, *Science* **2013**, *342*, 344.
- [42] E. Serpetzoglou, I. Konidakis, G. Kakavelakis, T. Maksudov, E. Kymakis, E. Stratakis, *ACS Appl. Mater. Interfaces* **2017**, *9*, 43910.
- [43] J. Kim, R. Godin, S. D. Dimitrov, T. Du, D. Bryant, M. A. McLachlan, J. R. Durrant, *Adv. Energy Mater.* **2018**, *8*, 1802474.
- [44] L. Kronik, Y. Shapira, *Surf. Interface Anal.* **2001**, *31*, 954.
- [45] D. Cavalcoli, A. Cavallini, *Phys. Status Solidi C* **2010**, *7*, 1293.
- [46] L. Kronik, Y. Shapira, *Surf. Sci. Rep.* **1999**, *37*, 1.
- [47] Y. J. Lee, J. Wang, J. W. P. Hsu, *Appl. Phys. Lett.* **2013**, *103*, 173302.
- [48] J. R. Harwell, T. K. Baikie, I. D. Baikie, J. L. Payne, C. Ni, J. T. S. Irvine, G. A. Turnbull, I. D. W. Samuel, *Phys. Chem. Chem. Phys.* **2016**, *18*, 19738.
- [49] S. Lee, D. Bin Kim, I. Hamilton, M. Daboczi, Y. S. Nam, B. R. Lee, B. Zhao, C. H. Jang, R. H. Friend, J. S. Kim, M. H. Song, *Adv. Sci.* **2018**, *5*, 1801350.
- [50] P. Caprioglio, F. Zu, C. M. Wolff, J. A. Márquez Prieto, M. Stolterfoht, P. Becker, N. Koch, T. Unold, B. Rech, S. Albrecht, D. Neher, *Sustain. Energy Fuels* **2019**, *3*, 550.
- [51] S. Dong, Y. Liu, Z. Hong, E. Yao, P. Sun, L. Meng, Y. Lin, J. Huang, G. Li, Y. Yang, *Nano Lett.* **2017**, *17*, 5140.
- [52] S. Wang, T. Sakurai, W. Wen, Y. Qi, *Adv. Mater. Interfaces* **2018**, *1800260*, 1.
- [53] J. S. Manser, P. V. Kamat, *Nat. Photonics* **2014**, *8*, 737.
- [54] B. N. Lee, S. Kirmayer, E. Edri, G. Hodes, D. Cahen, *J. Phys. Chem. Lett.* **2014**, *5*, 2408.
- [55] P. Calado, A. M. Telford, D. Bryant, X. Li, J. Nelson, B. C. O'Regan, P. R. F. Barnes, *Nat. Commun.* **2016**, *7*, 13831.

- [56] Y. Luo, P. Khoram, S. Brittan, Z. Zhu, B. Lai, S. P. Ong, E. C. Garnett, D. P. Fenning, *Adv. Mater.* **2017**, *29*, 1703451.
- [57] M. Daboczi, I. Hamilton, S. Xu, J. Luke, S. Limbu, J. Lee, M. A. McLachlan, K. Lee, J. R. Durrant, I. Baikie, J.-S. Kim, *ACS Appl. Mater. Interfaces* **2019**, *11*, 46808.
- [58] A. Pockett, G. E. Eperon, N. Sakai, H. J. Snaith, L. M. Peter, P. J. Cameron, *Phys. Chem. Chem. Phys.* **2017**, *19*, 5959.
- [59] T. Leijtens, G. E. Eperon, A. J. Barker, G. Grancini, W. Zhang, J. M. Ball, A. R. S. Kandada, H. J. Snaith, A. Petrozza, *Energy Environ. Sci.* **2016**, *9*, 3472.
- [60] V. W. Bergmann, Y. Guo, H. Tanaka, I. M. Hermes, D. Li, A. Klasen, S. A. Bretschneider, E. Nakamura, R. Berger, S. A. L. Weber, *ACS Appl. Mater. Interfaces* **2016**, *8*, 19402.
- [61] Q. Zhao, T. Xie, L. L. Peng, Y. Lin, P. Wang, L. L. Peng, D. Wang, *J. Phys. Chem. C* **2007**, *111*, 17136.